

**Fluidization dynamics of cohesive Geldart B particles. Part I  
X-ray tomography analysis**

Ma, Jiliang; van Ommen, J. Ruud; Liu, Daoyin; Mudde, Robert F.; Chen, Xiaoping; Wagner, Evert C.; Liang, Cai

**DOI**

[10.1016/j.cej.2018.11.082](https://doi.org/10.1016/j.cej.2018.11.082)

**Publication date**

2019

**Document Version**

Final published version

**Published in**

Chemical Engineering Journal

**Citation (APA)**

Ma, J., van Ommen, J. R., Liu, D., Mudde, R. F., Chen, X., Wagner, E. C., & Liang, C. (2019). Fluidization dynamics of cohesive Geldart B particles. Part I: X-ray tomography analysis. *Chemical Engineering Journal*, 359, 1024-1034. <https://doi.org/10.1016/j.cej.2018.11.082>

**Important note**

To cite this publication, please use the final published version (if applicable).  
Please check the document version above.

**Copyright**

Other than for strictly personal use, it is not permitted to download, forward or distribute the text or part of it, without the consent of the author(s) and/or copyright holder(s), unless the work is under an open content license such as Creative Commons.

**Takedown policy**

Please contact us and provide details if you believe this document breaches copyrights.  
We will remove access to the work immediately and investigate your claim.

***Green Open Access added to TU Delft Institutional Repository***

***'You share, we take care!' – Taverne project***

**<https://www.openaccess.nl/en/you-share-we-take-care>**

Otherwise as indicated in the copyright section: the publisher is the copyright holder of this work and the author uses the Dutch legislation to make this work public.



## Fluidization dynamics of cohesive Geldart B particles. Part I: X-ray tomography analysis



Jiliang Ma<sup>a,\*</sup>, J. Ruud van Ommen<sup>b</sup>, Daoyin Liu<sup>a</sup>, Robert F. Mudde<sup>b</sup>, Xiaoping Chen<sup>a</sup>, Evert C. Wagner<sup>b</sup>, Cai Liang<sup>a</sup>

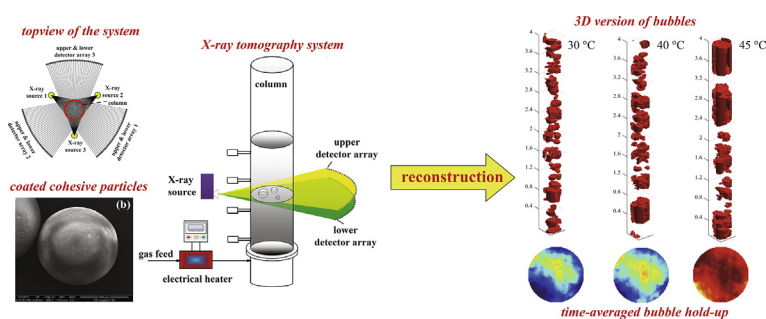
<sup>a</sup> Key Laboratory of Energy Thermal Conversion and Control of Ministry of Education, School of Energy and Environment, Southeast University, Sipailou No. 2, 210096 Nanjing, PR China

<sup>b</sup> Department of Chemical Engineering, Delft University of Technology, Van der Maasweg 9, 2629HZ Delft, The Netherlands

### HIGHLIGHTS

- X-ray tomography was used to reconstruct 3D bubbles in a bubbling bed.
- The inter-particle cohesive force facilitates the coalescence of bubbles in the bed.
- The fluidization fails as the whole bed slugging under large cohesive force.
- Bubble rise velocity sharply drops with the appearance of slugging.

### GRAPHICAL ABSTRACT



### ARTICLE INFO

#### Keywords:

Cohesive particle  
Fluidization  
X-ray tomography  
Bubble  
Slugging

### ABSTRACT

Due to the presence of inter-particle cohesive force, cohesive particles reveal totally different fluidization behaviors as compared to the non-cohesive system. This paper studies the fluidization dynamics of Geldart B particles with varying thermal-induced cohesive forces. Multi-source X-ray tomography was applied to reconstruct 3D temporal images of bubbles, based on which, various bubble properties were extracted. The results show that increasing cohesive force will decrease bubble number while increase bubble size, implying that the presence of cohesive force facilitates bubble coalescence. By examining the bubble size distribution, cohesive force is found to have no effect on the number of median bubbles but greatly influence small and large bubbles. When the cohesive force is strong, the bubbles grow to a considerable size similar with bed dimension, giving rise to slugging near bed surface. With the action of inter-particle cohesive force, particle slug gradually grows by capturing other freely fluidizing particles, finally inducing “whole-bed” slugging. The particle slug may rupture in the rising process, and the bed turns back to normal fluidization. In comparison to normal bubbles, the gas slug has much larger size but far smaller frequency. The rise velocity of gas slug is also very low due to the particle-wall friction and gas-solid momentum dissipation. Therefore, the averaged values of bubble properties dramatically changed as bed temperature exceeds 35 °C. When the temperature attains 45 °C, the cohesive force is so strong that the fluidization completely fails in terms of stable whole-bed slugging.

\* Corresponding author.

E-mail addresses: [jlma@seu.edu.cn](mailto:jlma@seu.edu.cn) (J. Ma), [J.R.vanOmmen@tudelft.nl](mailto:J.R.vanOmmen@tudelft.nl) (J.R. van Ommen), [dylu@seu.edu.cn](mailto:dylu@seu.edu.cn) (D. Liu), [r.f.mudde@tudelft.nl](mailto:r.f.mudde@tudelft.nl) (R.F. Mudde), [xpchen@seu.edu.cn](mailto:xpchen@seu.edu.cn) (X. Chen), [e.c.wagner@tudelft.nl](mailto:e.c.wagner@tudelft.nl) (E.C. Wagner), [liangc@seu.edu.cn](mailto:liangc@seu.edu.cn) (C. Liang).

<https://doi.org/10.1016/j.cej.2018.11.082>

Received 20 July 2018; Received in revised form 7 November 2018; Accepted 10 November 2018

Available online 12 November 2018

1385-8947/ © 2018 Elsevier B.V. All rights reserved.

## 1. Introduction

Fluidized beds are widely used in industrial processes for their vigorous heat and mass transfer and flexibility in handling particles continuously. In many applications of fluidized reactors, the particles are cohesive, (e.g. olefin polymerization [1], liquid waste combustion [2], granulation [3], and drying [4]). The presence of inter-particle cohesive force causes different fluidization dynamics in comparison to non-cohesive system [5,6]. Thus, it is attractive to obtain more insight into the underlying mechanisms, based on which the processing of cohesive particulate systems could be optimized.

Basically, the inter-particle cohesive force may exist in multiple forms in nature, such as van der Waals force [7–9], electrostatic force [10,11], liquid bridge force [12], and particle bridge force due to sintering [13]. Decades ago, people paid attention to these forces presenting in gas-solid fluidized bed [14]. Molerus declared that if the inter-particle forces is in the same order of magnitude as the particle gravity, the particle can be called sticky and the fluidization regime may be changed [15]. Seville and Clift further illustrated it by examining the behaviors of Geldart B particles at minimum fluidization status with liquid injection. As liquid amount increases, the fluidization characteristics transfer from group B to A and finally to C [14]. McLaughlin and Rhodes [16], and Wormsbecker [17] also found similar trends. In brief, the particles are more difficult to fluidize, because attenuation of kinetic energy arises upon particle collision [18] and the emulsion phase is prone to maintain a stable structure [19]. Then, extensive researches were carried out to study the fluidization dynamics of cohesive particles by changing the cohesive force within a low level. Most of them concerns minimum fluidization [20,21], fluidization regime [22] and particle behaviors [23–25]. As the cohesive force further increases, the particles would not rebound after collision [26], tending to adhere together and forms agglomerates [27]. Both the internal action from inter-particle cohesive force and the external action from particle collision and fluidization fluid determine the survival time of an agglomerate [28]. In some industrial applications, i.e., granulation, the dynamical balance between the internal and external actions is desired [3]. Nevertheless, if the cohesive force is stronger than those the fluid can impose on the particles, the balance would shift [29]. At this time, the agglomerate keeps growing and eventually causes partial or total defluidization of the bed [30].

Note that, the external action is closely related to bubble behaviors in a bubbling bed [31]. That is why the agglomerate shows different behaviors at different heights of the bed [32]. Therefore, it would be of great importance to investigate the bubble behaviors in a bubbling fluidized bed of cohesive particles.

There have been some studies concerning the bubbles in a cohesive bed. As the cohesive force increases, bubble size was found to increase first, because the emulsion phase has a higher capacity for holding the fluidizing gas inside its structure [33]. And then, the bubble size in turn increases [34]. Our early work also observed similar trends in a 2D fluidized bed [35]. The rising velocity and passage frequency of bubbles under different cohesive forces were also studied [36].

Due to the invisible nature of 3D bed, the existing studies collected bubble properties by means of pressure fluctuation analysis or optical fiber analysis, which only provide local and incomplete bubble information. This makes it difficult to relate the bubble behaviors to global fluidization status. Besides that, the way in which fluidization fails in a column of limited size is seldom reported. Accordingly, the relation between bubble behaviors and defluidization pattern is still unknown.

Aiming at the fluidization of cohesive Geldart B particles in a bubbling column, we used multi-source X-ray tomography to reconstruct 3D temporal image of bubbles and to extract bubble properties. Special attention was paid to the transition process of fluidization from vigorous status to defluidization. This paper analyzed the dependence of bubble dynamics on the cohesive force by examining the equivalent

diameter, rise velocity, frequency and spatial distribution of bubbles, and further built the relationship between the defluidization pattern and varying bubble behaviors.

## 2. Experimental description

### 2.1. X-ray tomography

The X-ray tomography system was developed at TU Delft. The measurement principle of X-ray tomography is transmission that could be described by Lambert-Beer law [37]:

$$I = I_0 e^{-\mu x} \quad (1)$$

where  $I_0$  and  $I$  are the intensity of X-ray lines before and after passing through a slab of material with thickness  $x$ ,  $\mu$  is the attenuation coefficient that depends on the property of materials. When scanning a fluidized bed with a fan beam of X-ray, the solid length that each X-ray line travels through could be calculated by measuring  $I$  and  $I_0$ .

As a non-intrusive and hard-field measurement method, X-ray tomography does not interfere with the internal flow of the bed, and the field lines of X-ray tomography are not influenced by the gas-solid distribution over the measurement plane [38]. Therefore, it is feasible to reconstruct the void distribution across the whole measurement plane if multiple X-ray sources are applied, based on which, 3D version of bubbles can be obtained [39,40]. Nevertheless, X-ray tomography cannot deal with high-density particles because of the excessive attenuation of X-ray radiation and the reconstruction is an iterative, off-line and time-consuming process [41]. Detailed comments on X-ray tomography as well as the comparison with other related experimental methods can be found in references [42,43].

### 2.2. Experimental setup

Fig. 1 shows the schematic of the experimental setup. The experiments were conducted in a Perspex column with an inner diameter of 0.14 m and a height of 1.6 m. The air distributor consists of a porous plate, sintered bronze with pore sizes ranging from 30 to 70  $\mu\text{m}$  and a thickness of 7 mm. The column was placed on a lifting table so that the scanned height could be adjusted by changing the table height. The static bed height is 300 mm. Three measurement heights of 70 mm, 150 mm and 230 mm from the gas distributor were investigated. Since the cohesive force is thermal-induced, we used fluidizing air to heat the bed materials to change the cohesive force between particles. By adjusting the temperature of fluidizing air, the particle temperature changes from 25 °C to 45 °C. The influence of temperature on air property was neglected because the experiment was performed in a narrow temperature range close to ambient so that the variance of air property is too small to affect the fluidization dynamics. Three fluidization gas velocities were examined, ranging from  $2 U_{mf}$  to  $3 U_{mf}$ .

Three X-ray sources were placed at 120° around the column. Each source generated a fan-beam X-ray whose intensity was measured by a detector array across the column. Each detector array consists of 2 rows of 32 detectors. The rows are spaced 4 cm apart, creating two measuring planes separated by approximately 1.09 cm at the location of the column. In total, there were 192 detectors around the column. The detector consisted of  $\text{CdWO}_4$  scintillation crystals (crystal size: 10 mm  $\times$  10 mm  $\times$  10 mm), optically coupled to a PIN photodiode (Hamamatsu S1337-1010BR type). The X-ray source was an YXLON Y.TU 160-D06 tube with a maximum voltage of 150 kV and a maximum current of 12 mA. Before the experiment, all source tubes had to be carefully aligned according to the investigated materials, to determine proper running voltage and current. The voltage and current of the source tubes determine the X-ray intensity. The intensity should not be too large or too small. If it is too small, the X-ray could not pass through the bed before complete attenuation. If too large, it will exceed the upper limit value that detector could receive. Generally, the proper

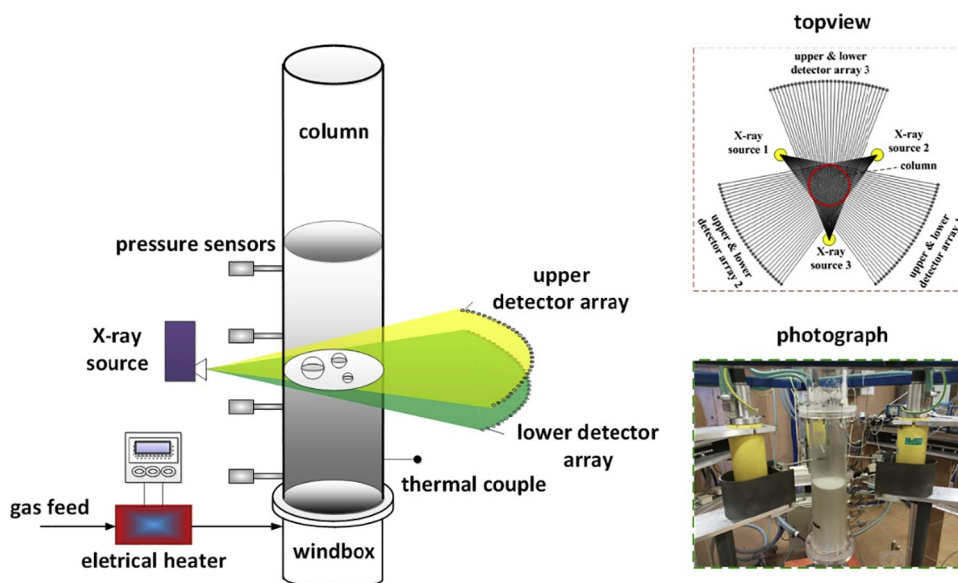


Fig. 1. Schematic of experimental setup.

intensity should satisfy two conditions: 1) the X-ray intensity should be large enough to be detected after passing through a **full** bed; 2) the X-ray intensity should not exceed the upper limit of detector after passing through an **empty** bed. So during the alignment, we adjusted the voltage and current of each source tube to motivate X-ray lines with different intensities, and checked the detector output to judge whether the above two conditions are met simultaneously. For the present work, the source tube settings were: source I:  $V_1 = 150$  kV,  $I_1 = 0.4$  mA; source II:  $V_2 = 150$  kV,  $I_2 = 1$  mA; source III:  $V_3 = 150$  kV,  $I_3 = 0.4$  mA. Due to the different natures of source tubes, the source II needs larger current to motivate X-ray lines with similar intensities to the other two. To ensure safety from the X-ray radiation, the setup was located in a room enclosed by lead walls. The on-off operation and data collection of the X-ray tomography was remotely controlled in the adjacent room. The output data of detectors was recorded for 1 min at a sampling frequency of 2500 Hz.

### 2.3. Materials

The approach of “polymer coating” was used to introduce the inter-particle cohesive force [44]. It was coating inert base particles with a polymer layer whose cohesiveness linearly depends on temperature [45]. The base particles were glass beads with a density of  $2500$  kg/m<sup>3</sup>. Before the experiment, the particles were carefully sieved for a narrow size distribution. The averaged diameter of the particles is  $600$   $\mu$ m, belonging to Geldart group B particles. Its minimum fluidization velocity,  $U_{mf}$ , was measured to be  $0.325$  m/s. Coating process was completed in a rotary coating machine for several batches for uniform coating. The polymer layer was the solidification outcome of the mixed solution (commercial name, Eudragit NE30D) of Poly ethyl acrylate (PEA) and poly methyl methacrylate (PMMA) around the particle surface. Fig. 2 shows the SEM images of glass bead surfaces before and after coating. In this work, the polymer layer thickness was controlled around  $10$   $\mu$ m. It is very thin relative to the particle diameter, so the influence of coating on the particle size could be neglected. Bouffard et al. found that the cohesive force between two coated particles increases almost linearly with the particle temperature, and proposed equations to predict the cohesive force. Based on this, the inter-particle cohesive force in the present work was roughly estimated. As the temperature increases from  $25$  °C to  $45$  °C, the cohesive force increases from 2.5 to 6 times particle gravity. Interested readers can go through the reference [45] for detailed information about the polymer layer

property.

### 2.4. Data processing

#### 2.4.1. Calibration

In order to convert the output of a detector to an amount of material, careful calibration is needed. The purpose of the calibration is to build a functional relation between the output of each detector and the solid length for the corresponding X-ray line. Fig. 3 shows the definition of solid length. It is the length of bed materials each X-ray line passes through.

The approach of calibration is placing a known amount of material in front of a detector and measuring the signal. Fig. 4 shows a snapshot of the calibration process and an example of the calibration curve. To reduce the influences from beam hardening of X-ray source tubes [39], a seven-point calibration was carried out. We started with an empty bed, scanning it for a short time (about 10 s). Then, a thin Perspex wall (1 mm in thickness) was placed into the column. The angle of the wall should be such that the walls are at  $90^\circ$  angle from the central line between source tube and detector. We filled up the compartment with materials and measured again. Then, remove the first wall, place a longer wall at next location, fill up with materials and repeat the measurement, until we had a full bed. At this time, no more walls are required and the seven-point calibration was completed.

Fig. 5 shows how to determine the solid length during calibration. Due to the fixed geometry of the partially filled column, the solid length of each X-ray line can be exactly calculated for each calibration point. Then, we plot a curve through the seven calibration points using the following equation based on Lambert-Beer law.

$$I = A + B \exp(-x/C) \quad (2)$$

where  $A$ ,  $B$  and  $C$  are the calibration coefficients,  $x$  is the calculated solid length,  $I$  is the detector output. Since  $I$  and  $x$  are known, the calibration coefficients can be easily calculated. Because the calibration coefficients largely depend on the nature of source tubes and detectors, all the 192 detectors and three tubes in the present study had to be calibrated respectively.

#### 2.4.2. Reconstruction

The objective of reconstruction was to obtain the void distribution over the measurement plane. The first step was taking the average of every 10 samples to reduce the noises from the raw signal. Although

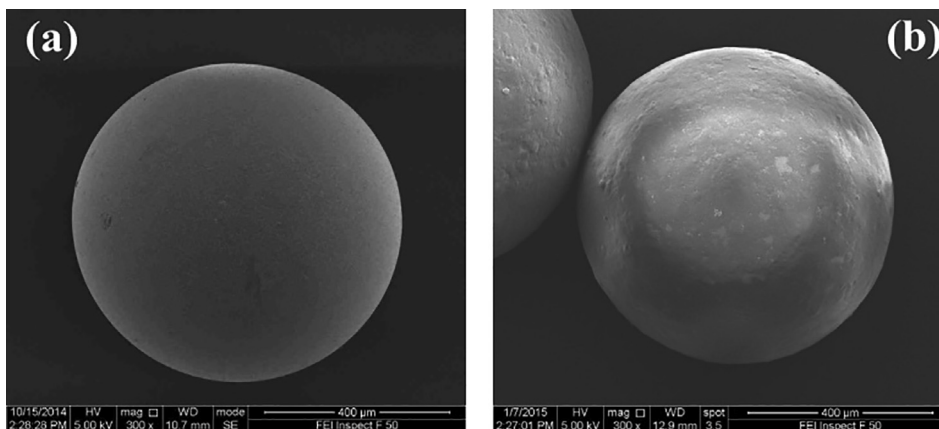


Fig. 2. SEM images of glass beads before and after coating. (a) uncoated particle, (b) coated particle.

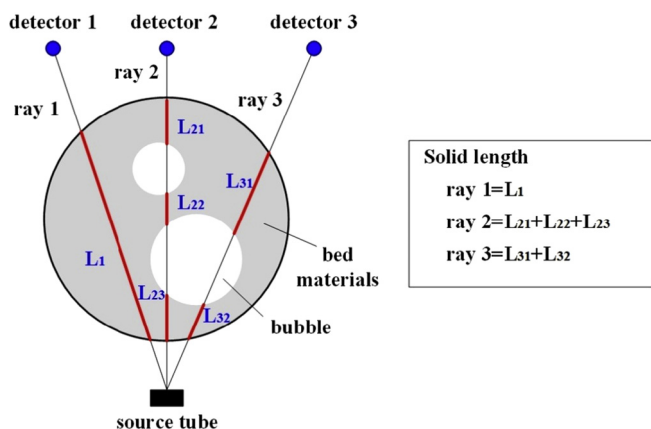


Fig. 3. Definition of solid length during fluidization.

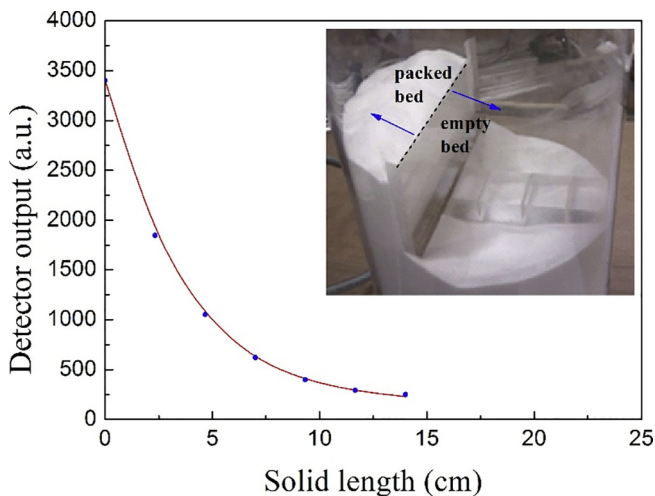


Fig. 4. Snapshot of calibration process and fitting curve for one detector.

this means a decline of actual sampling frequency from 2500 Hz to 250 Hz, the existing studies prove that this is adequate for analyzing fluidization dynamics [46]. The second step was converting the detector outputs into the path length for each X-ray line based on calibration results. The bed cross section was then discretized by a grid of  $50 \times 50$  pixels. An iterative reconstruction algorithm was applied to the solid length set to obtain the void fraction in each pixel, which appears as different gray levels [47]. The algorithm was a combination of Simultaneous Algebraic Reconstruction Technique (SART) and modified

One Step Late (OSL) method. Detailed description of the algorithm could be found in the reference of [41].

Fig. 6 shows an example of reconstructed gray-scale image from lower and upper measurement planes. The two white objectives in Fig. 6(a) and (b) are the cross sections of one bubble passing through both planes at the same time. Note that the boundary of the reconstructed objectives is blurred due to reconstruction errors. To obtain quantified information of bubbles, the reconstructed images were then binarized by thresholding all the pixels to convert the gray levels larger than the threshold value to 1, otherwise, to 0. Thus, determining an optimum threshold value is critical to the accuracy of quantified bubble properties.

In the present work, we scanned a settled bed inserted with a thin Perspex pipe of 52 mm I.D. By adjusting the threshold values applied to the reconstructed gray-scale image, the optimal threshold value was determined if the binary image provides the best area reproduction of the Perspex pipe. In this way, a threshold value of 0.68 was used for this work.

According to the previous studies, the uncertainties of binary voids of different sizes and locations have to be checked first before applying one threshold value to the entire 3D scanned domain [48,49]. Because X-ray tomography belongs to hard-field measurement, the presence of bed materials will not influence the direction of field lines. Therefore, the optimum threshold value will not change with the location of voids. Concerning the effects of void sizes, we compared the area of known pipes with that obtained via X-ray tomography. Fig. 7 shows the raw images for pipes of 52 mm I.D. and 28 mm I.D. inserting in a settled bed, as well as the corresponding binary images with the threshold value of 0.68. The pipe of 52 mm I.D. was reconstructed with more than 99% accuracy, while for the pipe of 28 mm I.D., the accuracy decreases to 90%. According to Rautenbach et al., the X-ray tomography has even higher uncertainties associated with small bubble sizes close to the spatial resolution limit [43]. Since the bubbles presenting in this work have comparatively large size, the reconstruction accuracy with threshold value of 0.68 is acceptable for the bubbling dynamic analysis.

By stacking the binary images chronologically, quasi-3D versions of bubbles passing through the measurement plane were obtained, as shown in Fig. 8. The vertical axis is time (in s) and the horizontal axis is the column dimension (in mm). Both measurement planes detected a sequence of bubbles with a similar shape and size, but slightly shifted in time of  $\Delta t$ . The bubble rise velocity was estimated as the ratio of distance between lower and upper planes to the time difference that the center of gravity of each individual bubble needs to pass both planes. Provided that the distance between two measurement planes in the bed center was 1.09 cm, the bubble rise velocity  $U_b$  could be calculated as  $U_b = 0.0109/\Delta t$ .

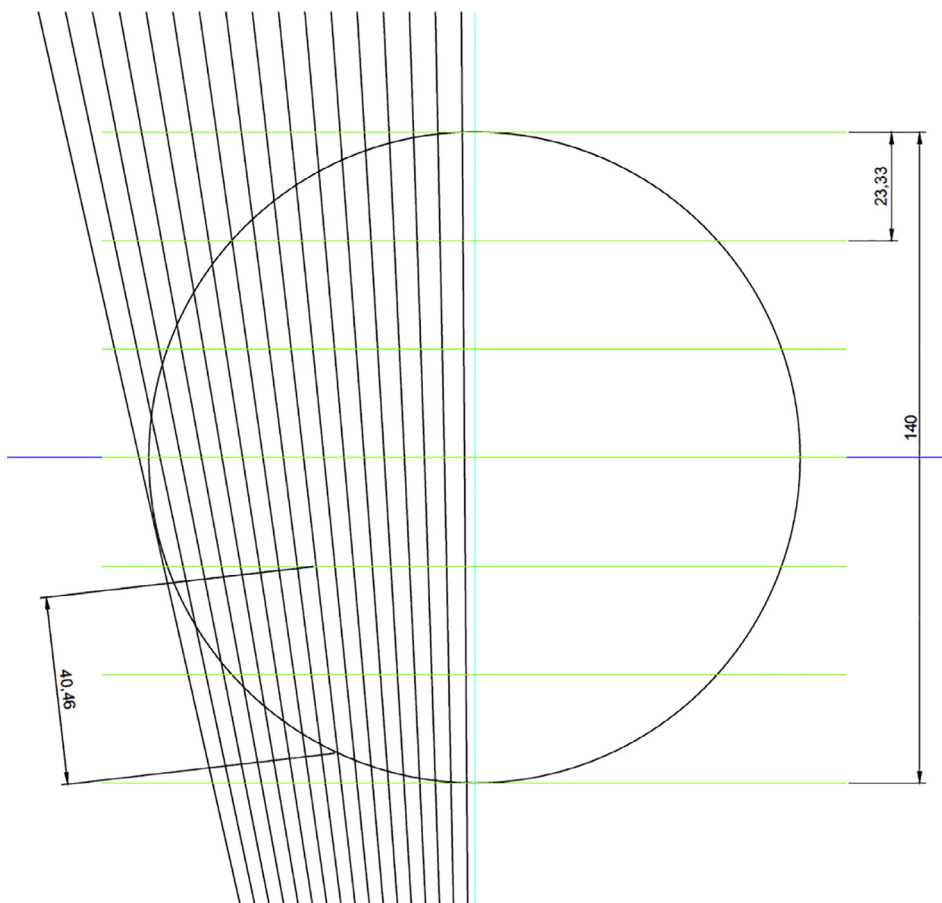


Fig. 5. Determination of the solid length values during the seven-point calibration. Green lines indicate wall locations, black lines mean X-ray lines travelling from source tube to detectors. (For interpretation of the references to colour in this figure legend, the reader is referred to the web version of this article.)

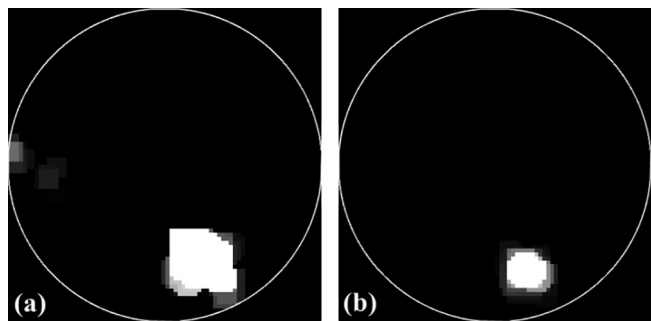


Fig. 6. Reconstructed gray-scale images for both planes. The white circle indicates the inner wall of the column. (a) lower plane; (b) upper plane.

### 3. Results and discussion

#### 3.1. Void fraction

Fig. 9 gives the time series of void fraction of bed cross section at the height of 150 mm. The void fraction represents the proportion of the bed cross section occupied by bubbles. At 30 °C, the void fraction frequently fluctuates below 0.75, indicating the ubiquity of small bubbles. As the temperature increases to 40 °C, the fluctuating frequency decreases and the amplitude increases, occasionally reaching 1. This implies that the whole cross section is occasionally occupied by bubbles. When the bed temperature reaches 45 °C, the void fraction frequently attains one, meaning that the complete occupation by bubbles is the dominant status.

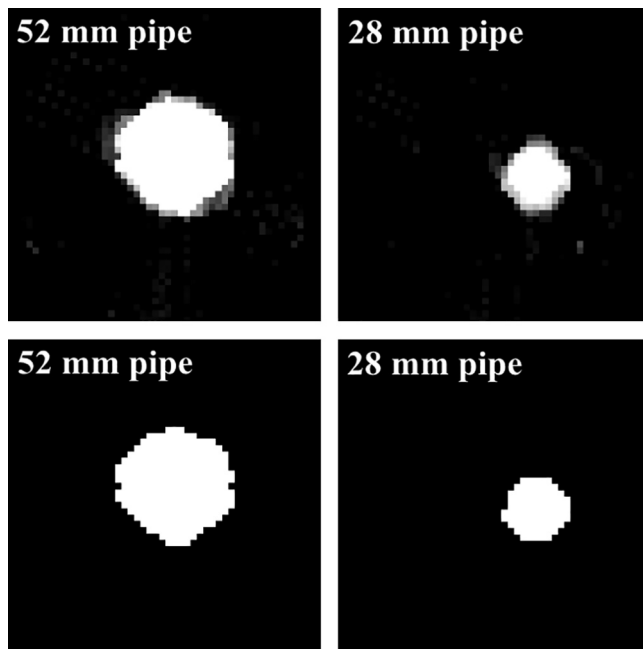


Fig. 7. Comparison of reconstructed images for settled bed inserted with known-size pipes. Top: raw images, bottom: thresholded images (threshold value 0.68).

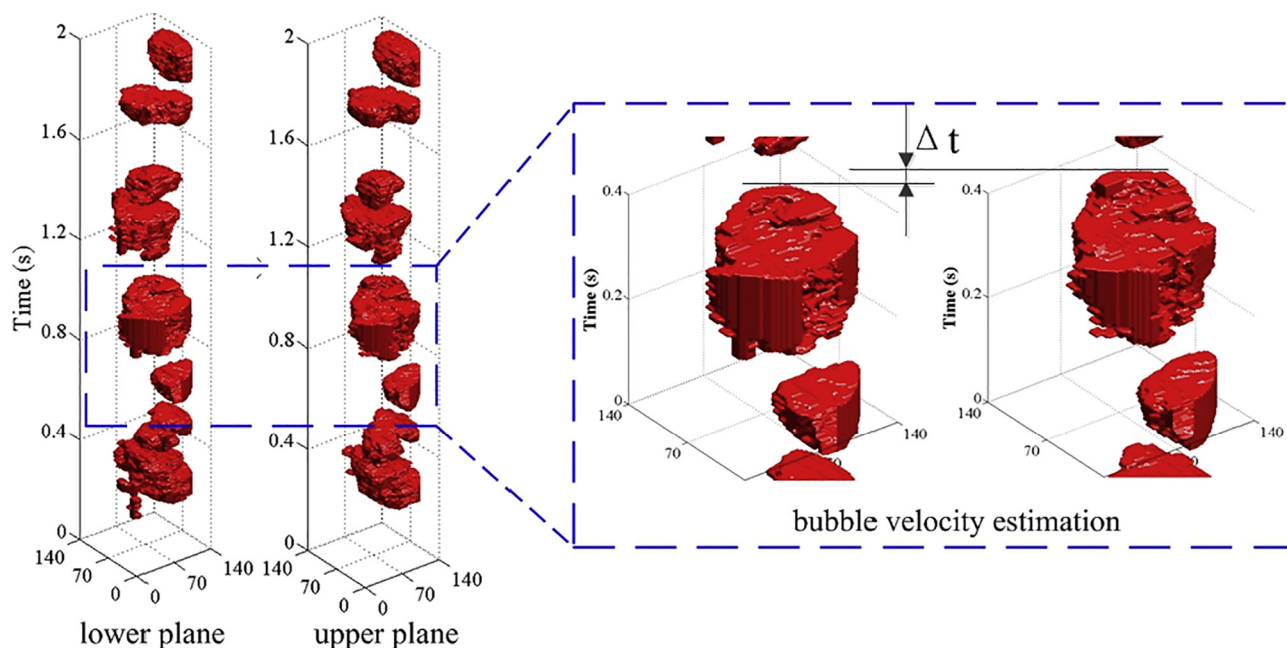


Fig. 8. Quasi-3D temporal image of bubbles (red objects) passing through both planes over 2 s and the schematic of bubble rise velocity estimation. (For interpretation of the references to colour in this figure legend, the reader is referred to the web version of this article.)

3.2. Reconstructed bubbles

Fig. 10 shows the 3D temporal image of bubbles at different measurement heights and cohesive forces. As shown in Fig. 10(a), many small bubbles are present and multi-bubble structure exists in terms of interlocking small bubbles at bottom bed [50], when cohesive force is small. As the cohesive force increases, less bubbles are observed, accompanied by a gradual growth of bubble size. With the further increase of the bed temperature to 45 °C, large bubbles with a dimension similar to the column cross section appear, pushing all the particles upward as a whole. This is so called “whole-bed slugging”. Such large bubble is named as “gas slug” and the particles above it is called “particle slug”. The particle slugs are prone to rupture if the external force from fluidized medium is larger than the inter-particle cohesive force. Therefore, the fluidization may turn back to normal status. According to the fluidization theory, bubble size should increase with measurement height [51]. However, this trend was not observed for the

temperature of 45 °C: the bubbles reconstructed at 230 mm are not as large as those observed at lower planes. This may be attributable to the rupture of particle slugs before reaching such great height. Later, quantitative information will be provided for further analysis. Overall, the presence of inter-particle cohesive force seems to enhance bubble growth, thus decreasing the specific area of bubbles and deteriorating the gas-solid mass transfer.

Fig. 11 gives the contour plots of the bubble hold-up over 1 min at different heights and cohesive forces. The three columns represent different cohesive forces: bed temperature equals 30 °C, 40 °C and 45 °C. The different rows represent the measurement height of 70 mm, 150 mm, 230 mm above the gas distributor. Different colors represent the time-averaged void fraction. The figure synthetically reflects the dimension and the number of bubbles passing through the cross sections. At the height of 70 mm, bubble hold-up increases with the cohesive force until 45 °C at which the whole cross section was nearly occupied by bubbles due to the frequent appearance of whole-bed

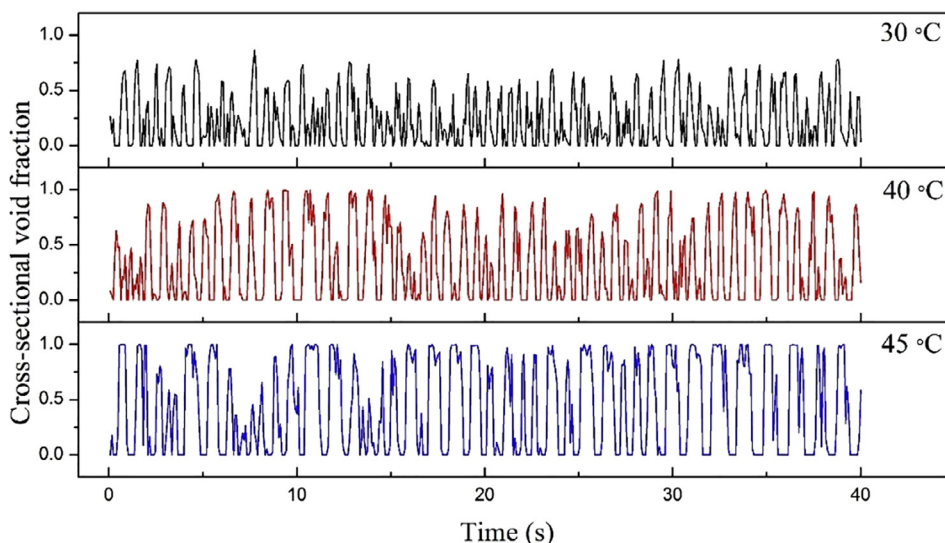


Fig. 9. Time series of void fraction on the cross section at the height of 150 mm and  $U_g = 2.5 U_{mf}$ .

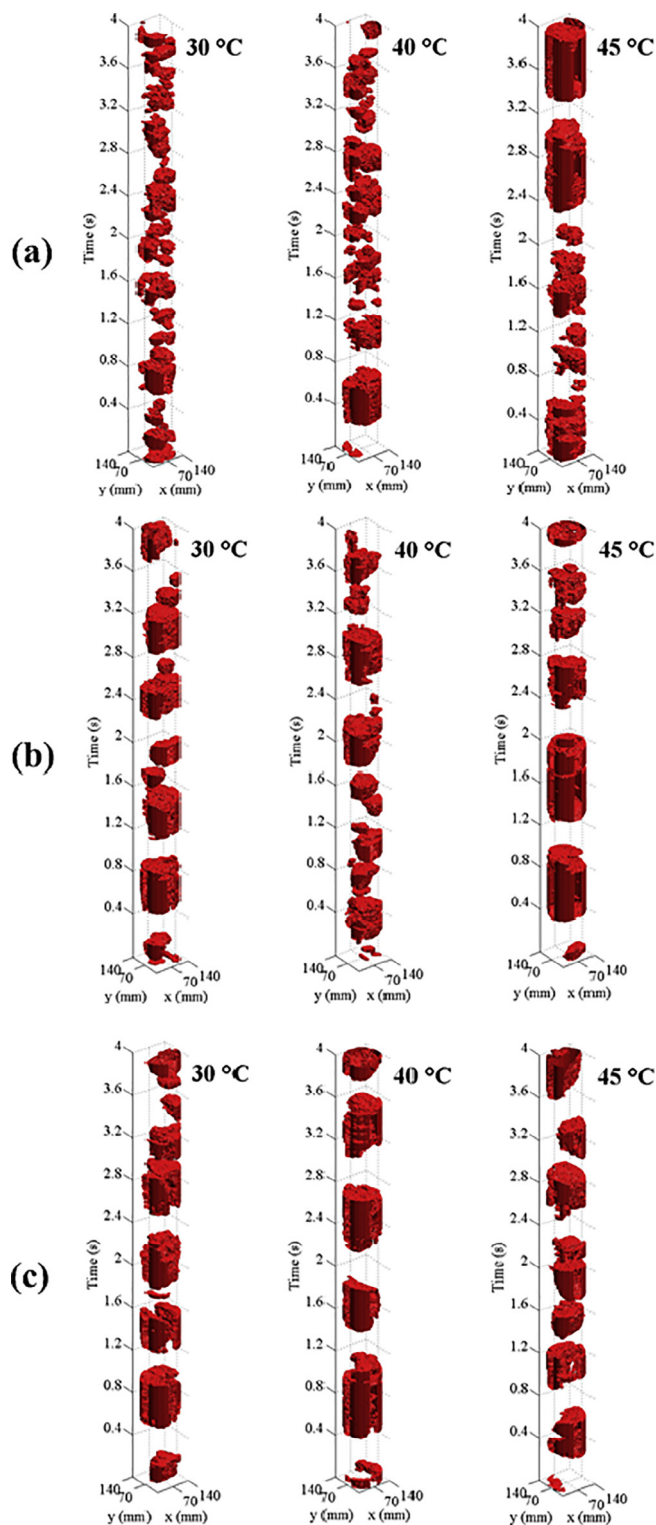


Fig. 10. 3D temporal image of reconstructed bubbles passing through the cross sections at different heights and cohesive forces for  $U_g = 2.5 U_{mf}$ . (a) 70 mm, (b) 150 mm, (c) 230 mm.

slugging. Interestingly, the largest bubble hold-up appears at 230 mm, 150 mm and 70 mm for the temperature of 30 °C, 40 °C and 45 °C respectively. Both normal bubbles and gas slugs determined the bubble hold-up. At 30 °C, no slugging appears. Therefore, the bubble hold-up follows the fluidization theory that larger bubbles present at higher heights. At 45 °C, slugging dominates fluidization and thus gas slug controls the bubble hold-up. Since the particle slug is more prone to

rupture at higher heights, the bubble hold-up tends to decrease with the elevation of measurement height.

Fig. 12 plots the distribution of bubble centroids over 1 min to reveal the preferred location of bubbles at different heights and cohesive forces. At the height of 70 mm, the bubbles are densely and homogeneously distributed, implying the presence of large amounts of small bubbles. With the elevation of the height, the bubble centroids move toward the bed center because the bubbles preferably rise from the bed corner to its center [52], meanwhile the bubbles distribute sparsely due to the decline of bubble numbers caused by bubble coalescence.

As the cohesive force increases, less bubbles were detected, therefore the distribution of bubble centroids at the same height become sparser. Moreover, the bubble centroids assemble around the bed center, particularly for the case of 45 °C at which most bubble centroids exactly fall upon the center point due to the presence of gas slugs. This feature was observed for all heights except 230 mm at which the distribution of bubble centroids scatters, indicating that less gas slugs present. This is consistent with the previous observation.

Above results are interpreted based on the reconstructed images, although straightforward, but lacking the quantitative information of bubbles that is still needed for the further insight into the effects of cohesive force. In the following, quantitative description of bubbles collected from reconstruction results are given.

### 3.3. Bubble frequency

Fig. 13 shows the time-averaged bubble frequency at different heights and cohesive forces. Bubble frequency represents the number of bubbles passing through the measurement plane per second. As expected, bubble frequency decreases with the measurement height due to bubble coalescence. As the cohesive force increases, bubble frequency slightly decreases until 35 °C. Beyond 35 °C, bubble frequency rapidly decreases. The underlying mechanisms for the decline of bubble frequency with cohesive force are probably different before and after 35 °C for very different decreasing rates. The sharp drop is related to the presence of whole-bed slugging. At 35 °C, the bubbles grow to a considerable size similar with bed dimension, giving rise to slugging near bed surface. With the action of inter-particle cohesive force, particle slug gradually grows by capturing other freely fluidizing particles, finally inducing “whole-bed” slugging. Taking 45 °C as an example, the whole-bed slugging takes place and dominates the fluidization by then. Different from the normal fluidization, the whole bed slugging collects all the inlet gas as one gas slug. Unless the slug ruptures, there will be only one bubble in bed, regardless of measurement height. Therefore, the bubble frequency at different heights are nearly the same at 45 °C.

### 3.4. Equivalent bubble diameter

Fig. 14 shows the effects of cohesive force on the time-averaged spherical equivalent bubble diameter (hereafter called ‘bubble diameter’) at different measurement heights. It is the diameter of sphere with the same volume to the reconstructed bubble. Similar to Fig. 13, two regions may be distinguished when taking 35 °C as a turning point. Below 35 °C, the bubble diameter gradually increases. Combining the fact that the bubble frequency decreases with increasing cohesive force, we can conclude that the presence of cohesive force facilitates bubble coalescence with limited effects. The following two reasons may be responsible for this phenomenon. First, the increasing cohesive force enhances the stability of emulsion phase so that fewer particles rain down from bubble roof as a ‘knife’ to split bubbles [53]. Second, less gas is allowed to enter the emulsion structure, causing that the additional fluidization gas is prone to appear in bubble phase and present as larger bubbles [36]. As the temperature increases beyond 35 °C, bubble diameter sharply rises because gas slug whose size is much larger than normal bubbles, present in bed and increase with cohesive force. At 45 °C, the bubble diameters at different heights are nearly the same,

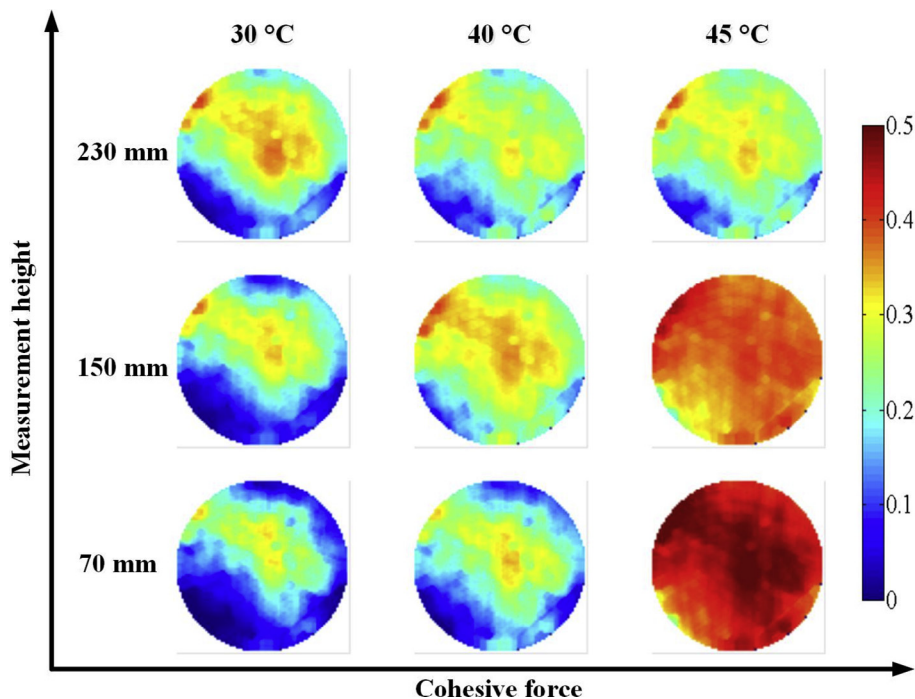


Fig. 11. Time-averaged bubble hold-up at different heights and cohesive forces for  $U_g = 2.5 U_{mf}$ .

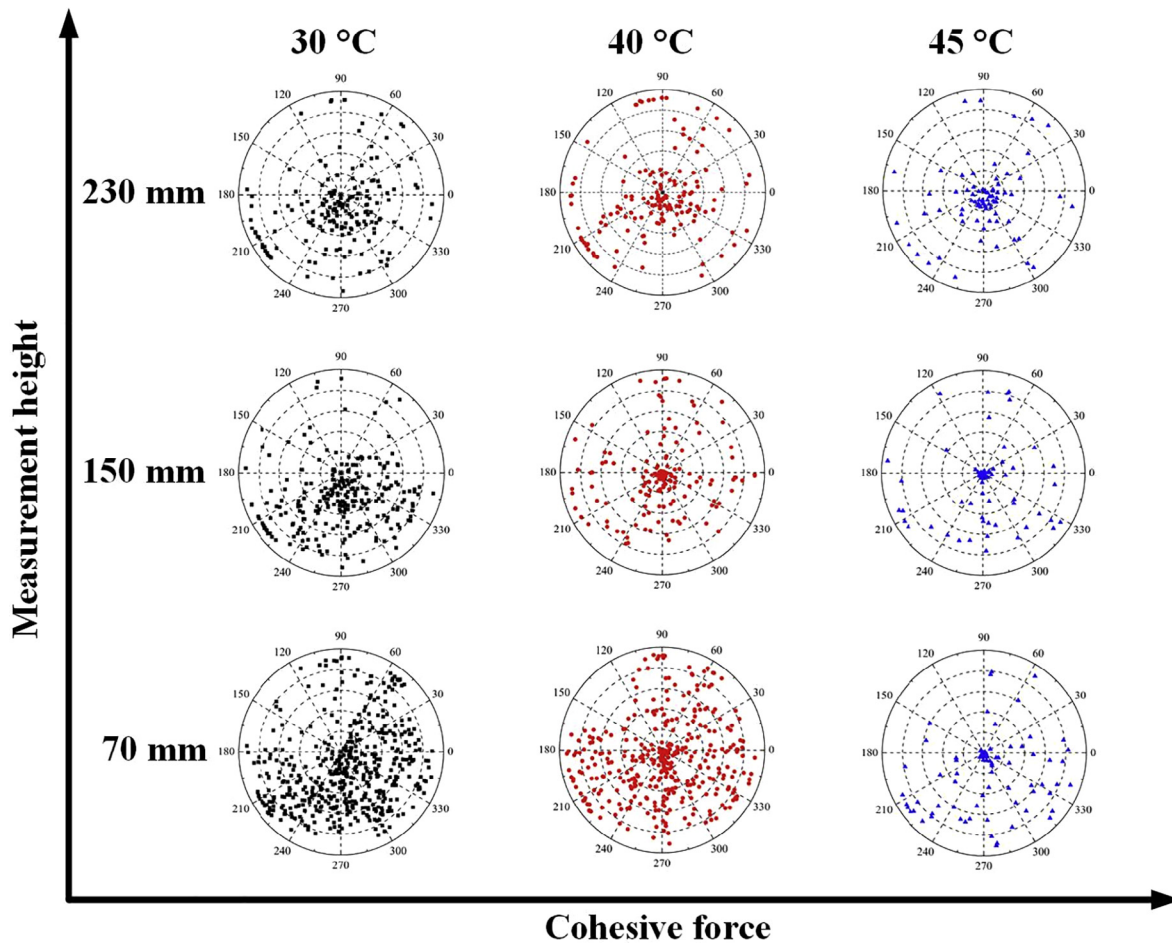


Fig. 12. Distribution of bubble centroids at different heights and cohesive forces for  $U_g = 2.5 U_{mf}$ .

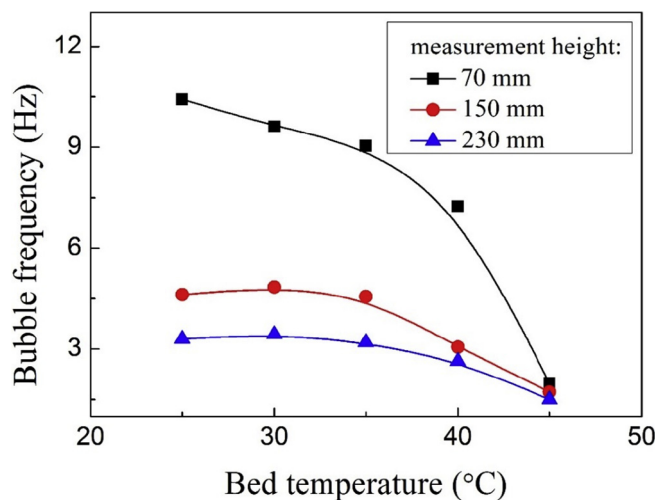


Fig. 13. Effects of cohesive force on the bubble frequency at different heights for  $U_g = 2.5 U_{mf}$ .

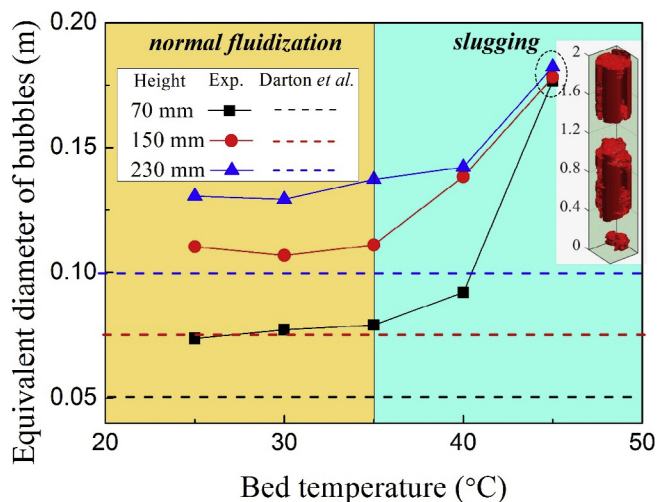


Fig. 14. Equivalent diameter of bubbles at different heights and cohesive forces for  $U_g = 2.5 U_{mf}$ .

following a similar trend with bubble frequency. That is because the bubbles detected are a mixture of normal bubbles and gas slugs. As the measurement height increases, the size of gas slug decreases due to the rupture of particle slug whereas the size of normal bubbles increases due to bubble coalescence. The two opposite trends are balanced so that the time-averaged bubble diameter at various heights are nearly the same. We also compared the experimental data with the theoretical prediction of Darton et al. [51], which was developed to predict the bubble size for non-cohesive bed. As seen, even at low cohesive case (25 °C), the bubble size is still much larger than non-cohesive bed. This indicates that the bubble size is very sensitive to the inter-particle cohesive force.

To further explore the evolution of bubbles, we studied the distribution of bubble size at the same condition of Fig. 14 and plotted the results in Fig. 15. At bottom bed (Fig. 15(a)), the bubbles detected under low cohesive force (30 °C) mainly consists of small bubbles whose diameters vary between 3 cm and 5 cm. The median bubbles take the second place, and the large bubbles (equivalent diameter around 15 cm) are the least. As the temperature increases to 40 °C, small bubbles sharply decreases, whereas the number of median bubbles changes a little because the coalescence between small bubbles and that between themselves are nearly balanced. Since the cohesive force promotes bubble coalescence, the bubbles larger than 15 cm first appear at

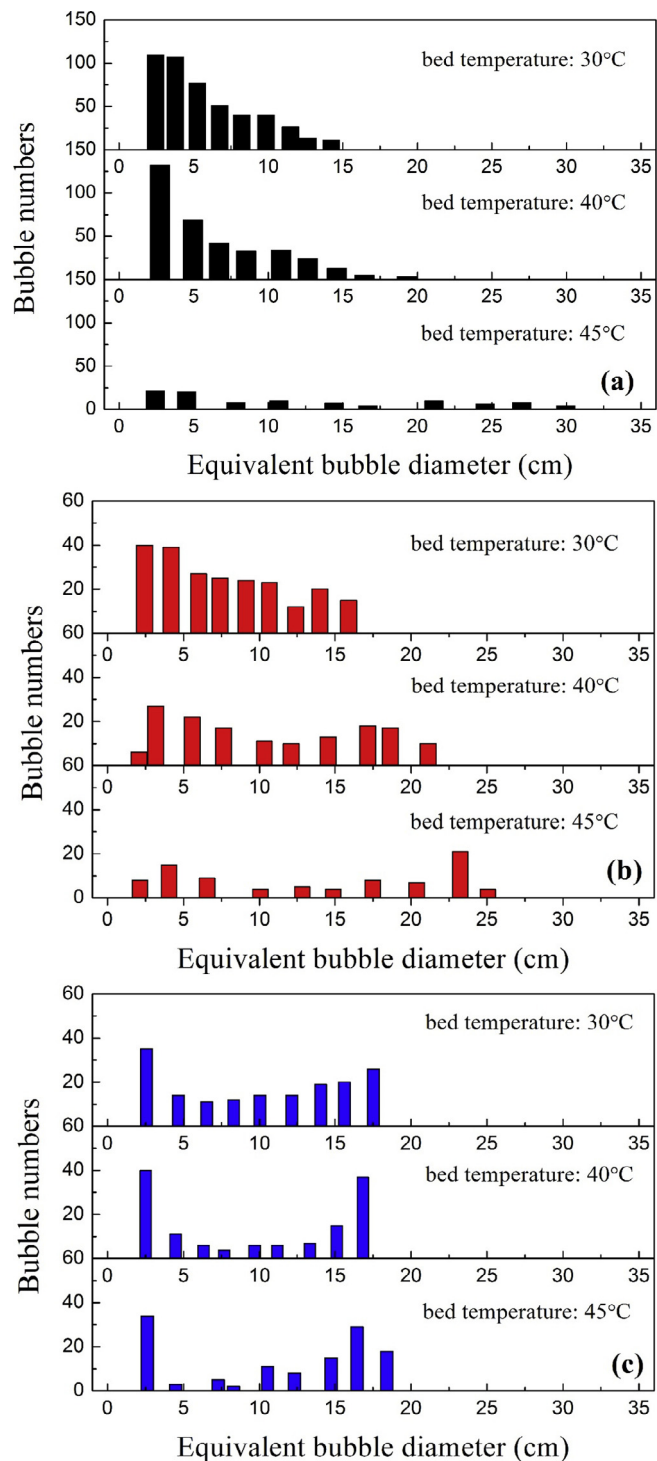


Fig. 15. Bubble size distribution at different heights and cohesive forces for  $U_g = 2.5 U_{mf}$ . (a) 70 mm, (b) 150 mm, (c) 230 mm.

40 °C. At 45 °C, few bubbles, with a flat distribution of bubble size, are observed. At this time, the bubble size is large enough to trigger slugging. Gas slugs with an equivalent diameter close to 30 cm are detected.

The bubble size distribution is bimodal at the heights of 150 mm (Fig. 15(b)) and 230 mm (Fig. 15(c)). This becomes more apparent with the increasing cohesive forces, as the median bubbles decreases. Even so, the averaged bubble diameter varies slightly as the temperature ranges below 35 °C (Fig. 14). This indicates that a balance forms between the coalescence and the rupture of median bubbles. The balance is broken with further increasing of the bed temperature to 45 °C.

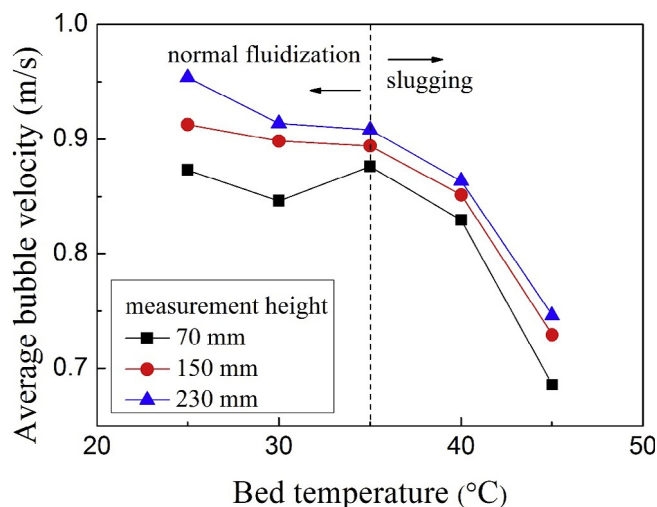


Fig. 16. Bubble rise velocity at different measurement heights and cohesive forces for  $U_g = 2.5 U_{mf}$ .

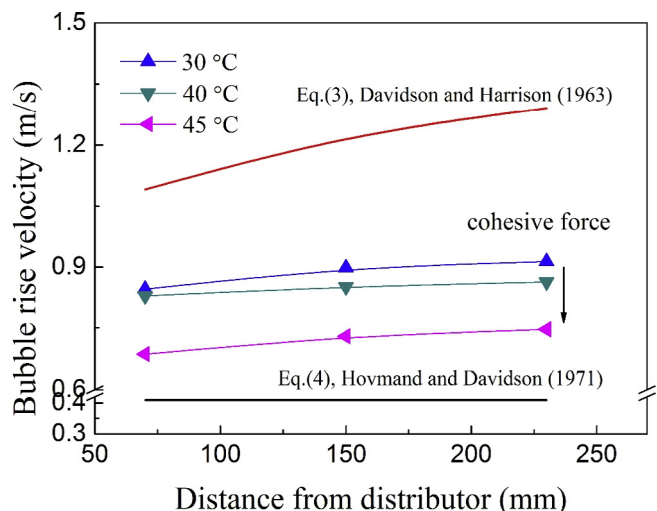


Fig. 17. Comparison between the experimentally and theoretically determined bubble rise velocity along the bed height for  $U_g = 2.5 U_{mf}$ .

Because higher heights have smaller bubble hold-up at 45 °C as shown in Fig. 11, less large bubbles are observed in Fig. 15(c).

### 3.5. Bubble rise velocity

Fig. 16 plots the bubble rise velocity at different heights and cohesive forces. As seen, the rise velocity decreases slightly with the cohesive force until 35 °C, because the increasing cohesive force enhances the stability of emulsion phase, thus enhancing the resistance for bubbles to rise. As the temperature increases beyond 35 °C, the bubble velocity sharply drops. This contradicts with standard fluidization theory that the rise velocity of bubbles proportionally depends on their sizes [54]. The unexpectedly decline of bubble velocity is attributed to the presence of slugs whose velocity is much smaller than normal bubbles due to the particle-wall friction and momentum dissipation from gas to the particles.

To better understand the dramatic change of bubble velocity, we compared the experimental data with the theoretical predictions from Davidson & Harrison [55] and Hovmand & Davidson [56], as shown in Fig. 17. The two empirical equations were proposed to predict the velocity of normal bubbles and single gas slug respectively:

$$U_b = U_g - U_{mf} + 0.71\sqrt{gD_b} \quad (3)$$

$$U_s = 0.35\sqrt{gD} \quad (4)$$

where  $U_b$  and  $U_s$  are the rising velocity of normal bubble and gas slug,  $g$  is the acceleration of gravity,  $D_b$  is the averaged equivalent bubble diameter obtained from experiment,  $D$  is the inner diameter of column.

Eq. (4) was applied, assuming that all the bubbles are slugs. Due to the effects of particle-wall friction and momentum dissipation from gas to the particles, the rise velocity of slug is much smaller than normal bubbles. Therefore, the prediction of Eq. (4) is the smallest, as shown in Fig. 17. Similarly, Eq. (3) assumes that all the bubbles are normal bubbles. According to the standard fluidization theory, the rise velocity of normal bubbles increases with their sizes. Therefore, the prediction of Eq. (3) is the largest. The bubbles detected in the experiment are actually a mixture of high-speed normal bubbles and low-speed gas slugs. Therefore, the experimental results fall within these extreme theoretical values. As the cohesive force increases, more gas slugs present in the bed, which will be discussed in detail in Part II. Consequently, the averaged bubble rise velocity gradually approaches to the theoretical value of single gas slug. That is why the bubble size increases while the bubble velocity decreases in the present work.

### 4. Concluding remarks

This paper used X-ray tomography to investigate the fluidization dynamics of Geldart B particles with varying inter-particle cohesive force. Special attention was given to the effects of cohesive force on bubble behaviors. Based on this, the defluidization pattern as well as the relation with bubble behaviors were studied. The following conclusions may be drawn:

- (1) Increasing cohesive force facilitates bubble coalescence, leading to an increase in bubble size and decline in bubble frequency.
- (2) As the cohesive force increases, the fluidization changes from normal status to an alternative process between normal fluidization and whole-bed slugging. When the temperature attains 45 °C, the cohesive force is so strong that the fluidization completely fails in terms of stable whole-bed slugging.
- (3) The averaged values of bubble properties including equivalent diameter, frequency and rise velocity dramatically changed as bed temperature exceeds 35 °C due to the presence of gas slugs.

### Acknowledgements

This work is supported by National Key R&D Program of China (2017YFB0603300) and National Nature Science Foundation of China (51806036 and 51676042).

### References

- [1] Z. Li, T.C.E. Janssen, K.A. Buist, N.G. Deen, M. van Sint Annaland, J.A.M. Kuipers, Experimental and simulation study of heat transfer in fluidized beds with heat production, *Chem. Eng. J.* 317 (2017) 242–257.
- [2] F. Micco, S. Kalisz, D. Baxter, K. Svoboda, Combustion of liquid bio-fuels in an internal circulating fluidized bed, *Chem. Eng. J.* 143 (2008) 172–179.
- [3] P. Suresh, I. Sreedhar, R. Vaidhiswaran, A. Venugopal, A comprehensive review on process and engineering aspects of pharmaceutical wet granulation, *Chem. Eng. J.* 328 (2017) 785–815.
- [4] V. Rimpilainen, L.M. Heikkinen, M. Vauhkonen, Moisture distribution and hydrodynamics of wet granules during fluidized-bed drying characterized with volumetric electrical capacitance tomography, *Chem. Eng. Sci.* 75 (2012) 220–234.
- [5] Y. Zhou, Q. Shi, Z. Huang, J. Wang, Y. Yang, Particle agglomeration and control of gas-solid fluidized bed reactor with liquid bridge and solid bridge coupling actions, *Chem. Eng. J.* 330 (2017) 840–851.
- [6] C.Q. LaMarche, P. Liu, K.M. Kellogg, C.M. Hrenya, Fluidized-bed measurements of carefully-characterized, mildly cohesive (Group A) particles, *Chem. Eng. J.* 310 (2017) 259–271.
- [7] D. Liu, B.G.M. van Wachem, R.F. Mudde, X. Chen, J.R. van Ommen, An adhesive CFD-DEM model for simulating nanoparticle agglomerate fluidization, *AIChE J.* 62 (2016) 2259–2270.

- [8] J.R. van Ommen, J.M. Valverde, R. Pfeffer, Fluidization of nanopowders: a review, *J. Nanopart. Res.* 14 (2012) 737–765.
- [9] H. Liu, L. Zhang, T. Chen, S. Wang, Z. Han, S. Wu, Experimental study on the fluidization behaviors of the superfine particles, *Chem. Eng. J.* 262 (2015) 579–587.
- [10] Y. Yang, S. Ge, Y. Zhou, J. Sun, Z. Huang, J. Wang, M. Lungu, Z. Liao, B. Jiang, Y. Yang, Effects of DC electric fields on meso-scale structures in electrostatic gas-solid fluidized beds, *Chem. Eng. J.* 332 (2018) 293–302.
- [11] J. Li, K. Kato, Effect of electrostatic and capillary forces on the elutriation of fine particles from a fluidized bed, *Adv. Powder Technol.* 12 (2001) 187–205.
- [12] Y. Zhou, Q. Shi, Z. Huang, J. Wang, Y. Yang, Z. Liao, J. Yang, Effects of interparticle forces on fluidization characteristics in liquid-containing and high-temperature fluidized beds, *Ind. Eng. Chem. Res.* 52 (2013) 16666–16674.
- [13] G. Tardos, R. Pfeffer, Chemical reaction induced agglomeration and defluidization of fluidized beds, *Powder Technol.* 85 (1995) 29–35.
- [14] J.P.K. Seville, R. Clift, The effect of thin liquid layers on fluidisation characteristics, *Powder Technol.* 37 (1984) 117–129.
- [15] O. Molerus, Interpretation of Geldart type-A, type-B, type-C and type-D powders by taking into account interparticle cohesion force, *Powder Technol.* 33 (1982) 81–87.
- [16] L.J. McLaughlin, M.J. Rhodes, Prediction of fluidized bed behaviour in the presence of liquid bridges, *Powder Technol.* 114 (2001) 213–223.
- [17] M. Wormsbecker, T. Pugsley, The influence of moisture on the fluidization behaviour of porous pharmaceutical granule, *Chem. Eng. Sci.* 63 (2008) 4063–4069.
- [18] T. Wang, Y. He, T. Tang, W. Peng, Experimental and numerical study on a bubbling fluidized bed with wet particles, *AIChE J.* 62 (2016) 1970–1985.
- [19] J. Shabnian, J. Chaouki, Effects of temperature, pressure, and interparticle forces on the hydrodynamics of a gas-solid fluidized bed, *Chem. Eng. J.* 313 (2017) 580–590.
- [20] D. Escudero, T.J. Heindel, Minimum fluidization velocity in a 3D fluidized bed modified with an acoustic field, *Chem. Eng. J.* 231 (2013) 68–75.
- [21] Y.T. Makkawi, P.C. Wright, Tomographic analysis of dry and semi-wet bed fluidization: the effect of small liquid loading and particle size on the bubbling behavior, *Chem. Eng. Sci.* 59 (2004) 201–213.
- [22] H. Xu, W. Zhong, B. Jin, J. Wang, Flow pattern and transition in gas-liquid-solid three phase spouted bed, *Powder Technol.* 267 (2014) 18–25.
- [23] H. Xu, W. Zhong, A. Yu, Z. Yuan, Spouting characteristics of wet particles in a conical-cylindrical spouted bed, *Ind. Eng. Chem. Res.* 54 (2015) 9894–9902.
- [24] Y. Zhou, Q. Shi, Z. Huang, J. Wang, Y. Yang, Effects of liquid action mechanisms on hydrodynamics in liquid-containing gas–solid fluidized bed reactor, *Chem. Eng. J.* 285 (2016) 121–127.
- [25] C.M. Boyce, A. Ozel, J. Kolehmainen, S. Sundaresan, C.A. McKnight, M. Wormsbecker, Growth and breakup of a wet agglomerate in a dry gas-solid fluidized bed, *AIChE J.* 63 (2017) 2520–2527.
- [26] P. Liu, K.M. Kellogg, C.Q. LaMarche, C.M. Hrenya, Dynamics of singlet-doublet collisions of cohesive particles, *Chem. Eng. J.* 324 (2017) 380–391.
- [27] J. Shabnian, J. Chaouki, Influence of interparticle forces on solids motion in a bubbling gas-solid fluidized bed, *Powder Technol.* 299 (2016) 98–106.
- [28] F. Parveen, C. Briens, F. Berruti, J. McMillan, Effect of particle size, liquid content and location on the stability of agglomerates in a fluidized bed, *Powder Technol.* 237 (2013) 376–385.
- [29] J. Gomez-Hernandez, D. Serrano, A. Soria-Verdugo, S. Sanchez-Delgado, Agglomeration detection by pressure fluctuation analysis during *Cynara cardunculus* L. gasification in a fluidized bed, *Chem. Eng. J.* 284 (2016) 640–649.
- [30] M. Bartels, W. Lin, J. Nijenhuis, F. Kapteijn, J.R. van Ommen, Agglomeration in fluidized beds at high temperatures: mechanisms, detection and prevention, *Prog. Energy Combust. Sci.* 34 (2008) 633–666.
- [31] F. Parveen, S. Josset, C. Briens, F. Berruti, Effect of size and density on agglomerate in a fluidized bed, *Powder Technol.* 231 (2012) 102–111.
- [32] S. Weber, S. Josset, C. Briens, F. Berruti, M. Gray, Predicting agglomerate fragmentation and agglomerate material survival in fluidized beds, *Powder Technol.* 210 (2011) 87–102.
- [33] J. Shabnian, J. Chaouki, Hydrodynamics of a gas-solid fluidized bed with thermally induced interparticle forces, *Chem. Eng. J.* 259 (2015) 135–152.
- [34] J. Shabnian, J. Chaouki, Fluidization characteristics of a bubbling gas–solid fluidized bed at high temperature in the presence of interparticle forces, *Chem. Eng. J.* 288 (2016) 344–358.
- [35] J. Ma, D. Liu, X. Chen, Bubble behaviors of large cohesive particles in a 2D fluidized bed, *Ind. Eng. Chem. Res.* 55 (2016) 624–634.
- [36] J. Shabnian, J. Chaouki, Local characterization of a gas-solid fluidized bed in the presence of thermally induced interparticle forces, *Chem. Eng. Sci.* 119 (2014) 261–273.
- [37] J. van den Eijnde, M. Schouwenburg, Practical Radiation Protection, Syntax Media, Utrecht, Netherland, 2013.
- [38] J. Saayman, W. Nicol, J.R. van Ommen, R.F. Mudde, Fast X-ray tomography for the quantification of the bubbling-, turbulent- and fast fluidization-flow regimes and void structures, *Chem. Eng. J.* 234 (2013) 437–447.
- [39] R.F. Mudde, Bubbles in a fluidized bed: a fast X-ray scanner, *AIChE J.* 57 (2011) 2684–2690.
- [40] X. Yang, J.R. van Ommen, R.F. Mudde, Gas distribution of a downward micro-nozzle assisted fluidized bed of fine powder, *Chem. Eng. J.* 264 (2015) 945–953.
- [41] R.F. Mudde, Double X-ray tomography of a bubbling fluidized bed, *Ind. Eng. Chem. Res.* 49 (2010) 5061–5065.
- [42] J.R. van Ommen, R.F. Mudde, Measuring the gas-solids distribution in fluidized beds – A review, *Int. J. Chem. React. Eng.* 6 (2008) 77–90.
- [43] C. Rautenbach, R.F. Mudde, X. Yang, M.C. Melaaen, B.M. Halvorsen, A comparative study between electrical capacitance tomography and time-resolved X-ray tomography, *Flow Meas. Instrum.* 30 (2013) 34–44.
- [44] J. Shabnian, J. Fotovat, J. Chaouki, J. Bouffad, Fluidization behavior in a gas-solid fluidized bed with thermally induced inter-particle forces, in: *10th International Conference on Circulating Fluidized Beds and Fluidization Technology – CFB-10*, T. Knowlton (PSRI Eds.), ECI Symposium Series, New York, 2013, 738–745.
- [45] J. Bouffard, F. Bertrand, J. Chaouki, Control of particle cohesion with a polymer coating and temperature adjustment, *AIChE J.* 58 (2012) 3685–3696.
- [46] G.C. Brouwer, E.C. Wagner, J.R. van Ommen, R.F. Mudde, Effects of pressure and fines content on bubble diameter in a fluidized bed studied using fast X-ray tomography, *Chem. Eng. J.* 207–208 (2012) 711–717.
- [47] R.A. Brooks, G. DiChiro, Principles of computer assisted tomography (CAT) in radiographic and radioisotopic imaging, *Phys. Med. Biol.* 21 (1975) 689–732.
- [48] V. Agrawal, Y.H. Shinde, M.T. Shah, R.P. Utikar, V.K. Pareek, J.B. Joshi, Estimation of bubble properties in bubbling fluidized bed using ECVT measurements, *Ind. Eng. Chem. Res.* 57 (2018) 8319–8333.
- [49] X. Li, A.J. Jaworski, X. Mao, Bubble size and bubble rise velocity estimation by means of electrical capacitance tomography within gas-solids fluidized beds, *Measurement* 117 (2018) 226–240.
- [50] H. Azizpour, R. Sotudeh-Gharebagh, N. Mostoufi, R. Zarghami, Characterization of regime transition in fluidized beds at high velocities by analysis of vibration signals, *Ind. Eng. Chem. Res.* 51 (2012) 2855–2863.
- [51] R.C. Darton, Bubble growth due to coalescence in fluidized beds, *Trans. Inst. Chem. Eng.* 55 (1977) 274–280.
- [52] J. Werther, O. Molerus, The local structure of gas fluidized beds II. The spatial distribution of bubbles, *Int. J. Multiphase Flow* 1 (1973) 123–138.
- [53] R. Clift, J.R. Grace, The mechanism of bubble break-up in fluidised beds, *Chem. Eng. Sci.* 27 (1972) 2309–2310.
- [54] S. Maurer, D. Gschwend, E.C. Wagner, T.J. Schildhauer, J.R. van Ommen, S.M.A. Biollaz, R.F. Mudde, Correlating bubble size and velocity distribution in bubbling fluidized bed based on X-ray tomography, *Chem. Eng. J.* 298 (2016) 17–25.
- [55] J.F. Davidson, D. Harrison, Fluidized Particles, Cambridge University Press, Cambridge, 1963.
- [56] S. Hovmand, J.F. Davidson, Pilot Plant and Laboratory Scale Fluidized Reactors at High Gas Velocities: The Relevance of Slug Flow, in: J.F. Davidson, D. Harrison (Eds.), Fluidization, Academic Press, London, 1971, p. 183.